Real Time Modulation of Hydrogen Evolution Activity of Graphene Electrodes Using Mechanical Strain

Min A Kim,[†] Dan C. Sorescu,[‡,§] Shigeru Amemiya,[†] Kenneth D. Jordan[†,§,*], and Haitao Liu[†,*]

[†]Department of Chemistry, University of Pittsburgh, Pittsburgh, Pennsylvania, 15260, United States

[‡]National Energy Technology Laboratory, United States Department of Energy, Pittsburgh, Pennsylvania 15236, United States

[§]Department of Chemical and Petroleum Engineering, University of Pittsburgh, Pittsburgh, Pennsylvania 15261, United States

*Corresponding Authors: hliu@pitt.edu (HL) and jordan@pitt.edu (KDJ)

Abstract

This paper reports the effect of mechanically applied elastic strain on the hydrogen evolution reaction (HER) activity of graphene under acidic conditions. Applied tensile strain of 0.2% on a graphene electrode is shown to lead to a 1 ~ 3 % increase of HER current. Tensile strain increases HER activity while compressive strain decreases it. Density functional theory (DFT) calculations using a periodic graphene slab model show increasing in the adsorption energy of H atom with growing tensile strain, leading to a corresponding enhancement of current density in HER, similar to that observed experimentally.

Introduction

The chemical properties of mechanically strained surfaces can differ significantly from their unstrained counterparts. Strain changes the lattice constant of the substrate, which could lead to a corresponding change in the energy of adsorption of atoms and molecules onto the surface.[1, 2] The effect of

strain on the reactivity of metal surfaces is of great interest in catalyst development. Specifically, the effect of strain on HER has been widely studied.[3-5] A major motivation of these studies is to improve the performance of existing HER catalyst.

Most bulk metals can only sustain 1% of elastic strain before plastic deformation occurs.[6] Applying strain to bulk materials is also inconvenient due to the large modulus of the metals, requiring significant amount of force. These issues limit the magnitude of the desired enhancement effect of strain as well as its applications in electrocatalysis. As an alternative, strain can also be introduced indirectly using lattice mismatch. It has been shown that growing a thin layer of metal on top of another metal that has a different lattice constant can create a strained surface.[7] However, this approach requires that the lattice mismatch must be small to allow epitaxial growth of the surface layer and there is no way to tune the strain in real time.

Carbon-based HER catalysts have attracted considerable interest in recent years due to its sustenability.[8] Graphene is also a particularly interesting target to probe the effect of extreme strain since it can withstand > 20% of tensile strain before fracture.[9] By comparison, most macroscopic single crystalline metals can only sustain <1% strain elastically. Therefore, graphene offers a unique testbed to explore real time, extreme modulations of electrocatalytic activities using strain engineering.

HER on graphene electrodes has been studied previously,[10, 11] and strain effects on the chemical reactivity of graphene itself have been studied and applied to functionalize graphene.[12, 13] However, the effect of strain on graphene towards its HER activity has not reported. Here, we report real time modulation of HER activity of graphene using mechanical strain. In particular, we show that tensile/compressive strain on graphene increases/decreases the current density of HER. DFT calculations show increasing adsorption energy of hydrogen with increasing tensile strain, leading to a reduction of the activation barrier of HER.

Results and Discussion

Mechanical Strain on Graphene. Tensile and compressive strain was applied to graphene supported on a flexible polymeric substrate. For this purpose, the graphene sample was transferred first to a polyethylene terephthalate (PET) substrate using a wet transfer method. In order to apply mechanical strain to graphene, the substrate was physically bent in either the outward or inward directions, leading to an applied tensile or compressive strain to graphene, respectively (Figure 1). The graphene sample used in this study is polycrystalline with a domain size on the order of 10s of microns, therefore, the strain effect discussed below is expected to be isotropic.

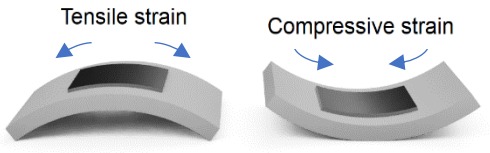

Figure 1. Schematics of strain application on a graphene/PET sample. Graphene (black) is placed on top of the PET substrate (gray). The PET substrate is bent outward/inward to induce tensile/compressive strain on the graphene.

The amount of mechanical strain applied to graphene via bending of the PET substrate was measured using Raman spectroscopy. Typical Raman spectra of graphene on PET are shown in Figure 2 along with the Raman spectrum of the PET substrate and of graphene on a SiO_2/Si substrate. The Raman spectrum of graphene has three major peaks: the D peak at ~1350 cm^{-1}, the G peak at ~1580 cm^{-1}, and the 2D peak at ~2700 cm^{-1}.[14] The 2D peak is sensitive to the mechanical strain.[14-17] A previous study of a graphene layer grown by chemical vapor deposition (CVD) showed that a strain of 1% results in a -72.3 cm^{-1} shift of the 2D peak.[18] We use the same Raman spectral dependency on strain when evaluating the change of strain in our sample.

A zero strain % (ε) was assigned to unbent PET supported samples while for the strained samples, the experimentally measured strain % was obtained relative to the unbent samples. Due to possible charge doping from the substrate/environments,[19] the initial amount of strain on an individual graphene/PET sample cannot be accurately measured based on the Raman 2D peak. The Raman spectrum of the PET substrate has several strong features below 1800 cm^{-1}, which hinders the analysis of the D and G peak regions. The maximum strain % applied to graphene throughout the experiment was ~ ±0.3 %, limited by the slippage between graphene and the PET substrate. The absolute strain % of graphene can vary between samples since the assigned zero strain condition could differ.

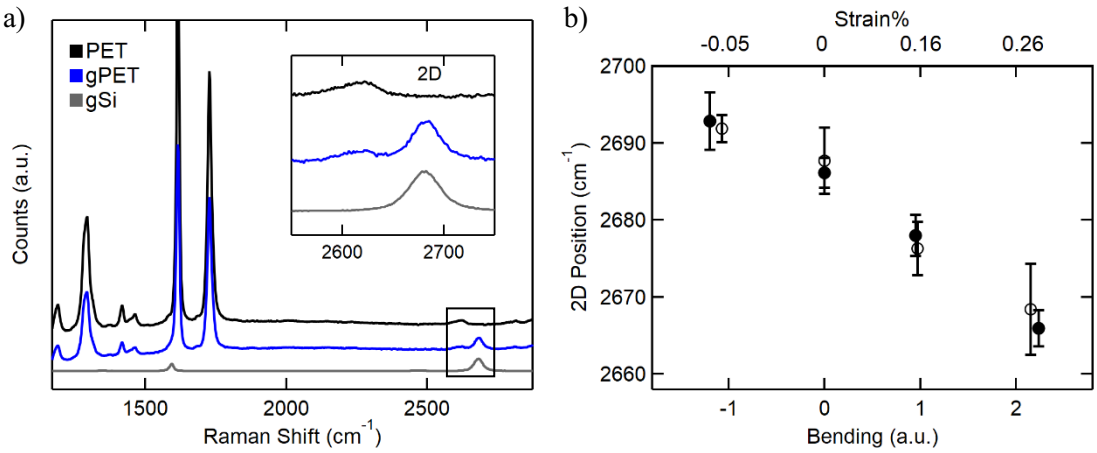

Figure 2. a) Raman spectra of PET substrate, graphene on PET, and graphene on Si wafer (from top to bottom). Insert shows a zoomed region of the PET peak at ~2620 cm^{-1} and the graphene 2D peak at ~2685 cm^{-1}. b) The position of the 2D peak of graphene with the bending amount of the substrate expressed in arbitrary units (a.u.) on the bottom axis. Top axis shows the corresponding graphene strain % calibrated from the 2D peak position shift. Two sets of Raman measurements (filled/empty symbols) are represented showing good reproducibility in the Raman data, in response to the applied strain.

The Effects of Strain on Graphene HER. The effects of strain on the measured current in HER can be determined using current-time measurements (Figure 3). The current was measured at a fixed potential (-0.5 V vs. Ag/AgCl) while the strain conditions were changed periodically. The apparent area of

graphene was optically measured at the initial unbent geometry to calculate the current density (J) for each current-time measurement. Tensile strains of 0, 0.17, and 0.25 % were applied. Each strain was applied and held for a period of 20 s. We observed a significant background drift in the current density, especially at the early stage of the experiment. This background drift of current density (dotted blue curve) varies between electrode samples, possibly due to non-uniform surface conditions of large area graphene (e.g., contaminants, defect density, grain size, etc.). For example, we previously showed that HOPG surface slowly adsorbs hydrocarbon contaminants in water, reducing its double layer capacitance and electrochemical activity.[20-23] The contaminants on the graphene surface can be also lifted off from the surface as H_2 gas bubbles form on the surface of graphene during HER. Nevertheless, despite the background drift of the current density throughout the measurements, a sharp change in current density is observed in response to the change in the applied strain (Figure 3a). A similar current response to the applied strain with negligible background drift is shown in Figure S1. Note that strain does introduce a very small change of the capacitance of the graphene electrode (several nF/cm^2). Any associated capacitive charging current should decay within 0.1 s; in contrast, the current change persists for 10s of seconds.

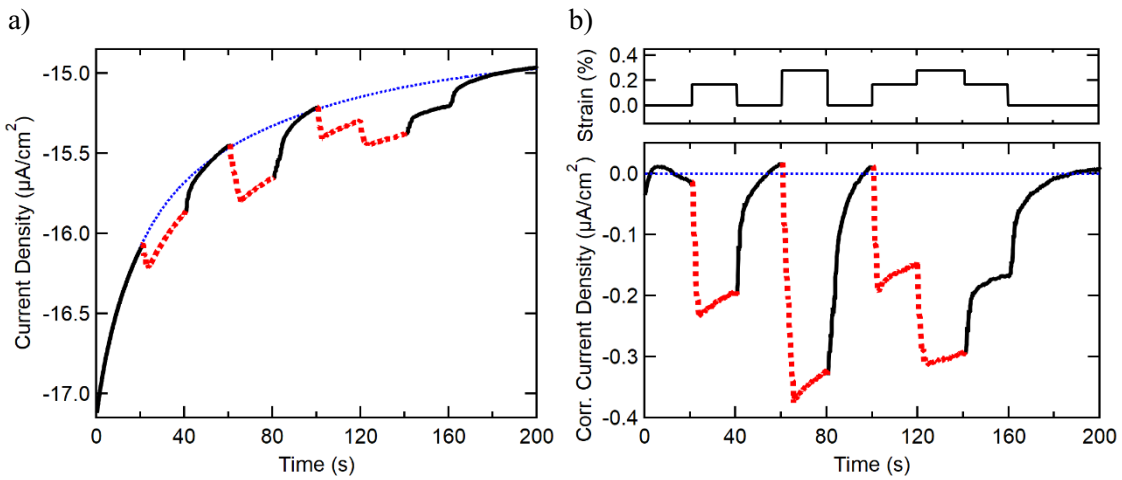

Figure 3. Measured current density of HER vs. time under constant potential (-0.5 V vs Ag/AgCl). a) Change in current density under tensile strain (dotted red). The overall shift of the current density is shown by a blue dotted line which was fitted with an exponential function over the range of values at zero strain%. b) Time variation of the current density with the background subtracted out (lower panel). Strain modulation sequence applied (upper subpanel). Note that a dip in the current density curve corresponds to an increase in the cathodic current.

The change in the current density (ΔJ) with strain can be visualized more clearly with the background subtracted out as shown in Figure 3b. Sharp and fast increase of the current density is seen under tensile strain. The magnitude of ΔJ was affected by the degree of strain%; larger tensile strain leads to larger ΔJ. Recovery of the current density (solid black) is clearly seen upon the relaxation of tensile strain. Interestingly, the kinetic behavior of the current density upon relaxation was slower compared to the change during the stretched period despite the absolute value of the rate of change in strain% remaining the same (manual bending and unbending action was done at the same rate). This slower change in current during the relaxation was also observed when compressive strain was applied (Figure S2). The removal of applied tensile strain results in a compressive directional force similar to that taking place upon application of a compressive strain.

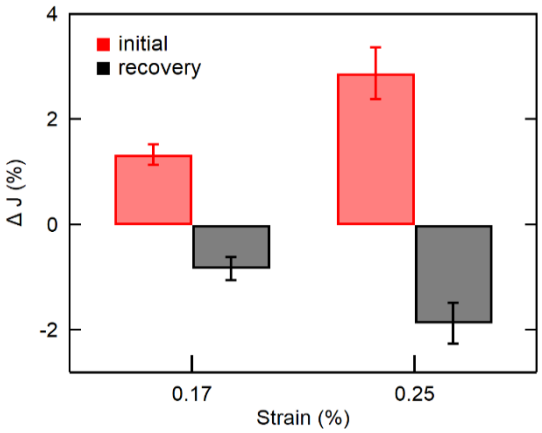

Figure 4. The change in current density under different amounts of tensile strain. There is a positive correlation between the strain and current change. The average increase in current under each strain is shown as positive change (initial). The average decrease in current upon the relaxation of each strain is shown as negative change (recovery).

The average percentage change in current density is shown in Figure 4. The effects of strain on HER current were collected repeatedly (24 times for 0.17 % and 8 times for 0.25 % tensile strain values) using multiple graphene electrodes. The change in current density values (ΔJ) were obtained from the difference between the current density before ($J_\circ$) and after (J_s) each strain application and expressed in percent variation relative to $J_\circ$. Because current density always increases with the tensile strain, initial ΔJ is positive ($J_s - J_\circ > 0$). The average initial ΔJ was 1.3 ± 0.2 % for 0.17 % tensile strain and 2.9 ± 0.5 % for 0.25 % tensile strain. Recovery of the current density was found from the change of current density upon the relaxation ($J_{\circ'}$) from the strained state (J_s) and expressed in percent variation relative to J_s. The recovery ΔJ ($J_{\circ'} - J_s < 0$) was averaged 64 % of initial ΔJ under tensile strain. Slow kinetic of current recovery after negative directional strain change might require a much longer time to reach equilibrium than the holding period used in the study, resulting in a lower estimate in the percent recovery. The surface of the graphene electrode could also partially undergo irreversible changes during the initial HER with tensile strain and

cause a smaller recovery amount. For example, polymer residues on the graphene surface can be removed curing HER via H_2 gas bubble forming between graphene and polymer interface or graphene can rupture if H_2 gas forms between graphene and supporting substrate.[11] Although such bubble formation was never visibly observed under the conditions used in this study, it is possible that HER could introduce additional defects over time, increasing activity with increased defect density (assuming defects favored HER) and/or increase of electrode area due to tear/lift of the graphene film from the substrate, both of which will make the observed strain-current effect pseudo-reversible.

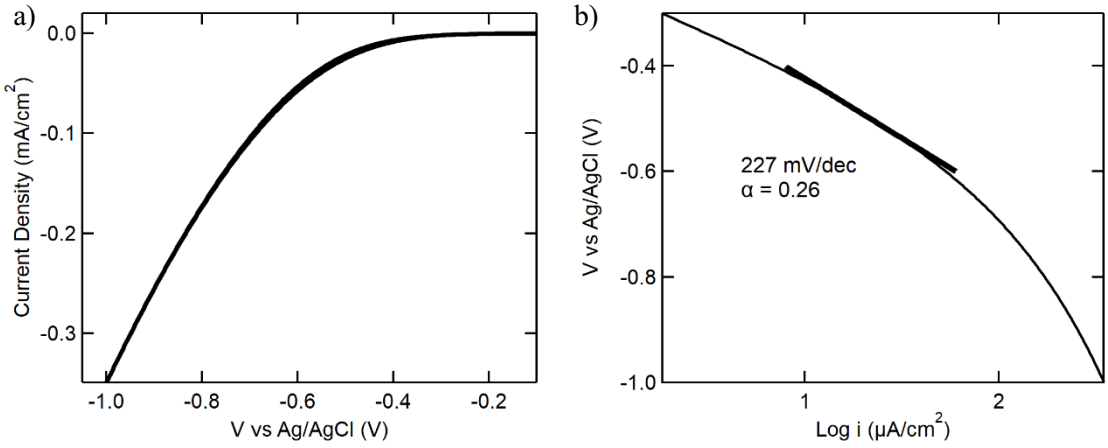

Figure 5. a) Cyclic voltammetry on graphene electrode in 0.5 M H_2SO_4. b) Tafel plot. All CVs were collected at scan rate of 0.1 V/s.

A typical cyclic voltammetry (CV) measurement on graphene electrode in 0.5 M H_2SO_4 is shown in Figure 5. The onset potential of HER was at around -0.4 V vs. Ag/AgCl. Increase in HER current under the tensile strain was also observed in CV measurements (Figure S3). The background drift observed in current-time measurement also persisted in the CV measurement, as a result, the effect of strain was less obvious due to the longer CV sampling interval. At -0.5 V, the Tafel slope and the transfer coefficient were 227 mV/decade and 0.26, respectively. The Tafel plot shows significant change in its slope depending on the potential. The Tafel slope increases as potential becomes more negative. The Tafel slope of ~690

mV/decade in the potential region < -0.8 V is found to be three times larger than the one of ~230 mV/decade around -0.5 V. It is generally accepted that HER occurs in following reaction steps:

Volmer $$M + H^+ + e^- \rightleftharpoons M-H \quad (1)$$

Heyrovsky $$M-H + H^+ + e^- \rightleftharpoons H_2 \quad (2)$$

Tafel $$2(M-H) \rightleftharpoons 2M + H_2 \quad (3)$$

where M denotes an available adsorption site on the electrocatalyst surface. The change of the Tafel slope by a factor of 3 at more negative potentials has been predicted theoretically when the Heyrovsky reaction is the rate-determining step.[24]

The change of the Tafel slope observed here suggests that HER on graphene electrode used in this study proceeds through the Volmer-Heyrovsky pathway. However, the absolute values of Tafel slopes are much larger than those theoretically calculated (120, 40, and 30 mV/decade for the rate determining steps of Volmer, Heyrovsky, and Tafel respectively). Various Tafel slopes of graphene electrode have been reported previously, ranging from 147 mV/decade[10] to 234 mV/decade.[11] The use of different substrates in the different studies could be the reason the variation in the different reported values of the Tafel slope of graphene. The effects of underlaying substrates on the electronic properties of graphene such as substrate induced doping of graphene are well-known.[25, 26]

The measured HER current reflects the kinetics of H^+ reduction on the electrode surface when the concentration of H^+ near the surface has not been depleted. The current density is very low (< 1 mA/cm^2) for 1 M of H^+, suggesting that the diffusion of H^+ to the electrode surface has negligible effects on the current. Therefore, the observed current change should be independent of the changes in surface roughness (e.g., flattening wrinkles under tensile strain) and geometry (e.g., curved shape due to the bending motion). Based on the pseudo-reversible response of the current as a function of applied strain, we believe that strain-induced damage (e.g., new defects, change of surface area) on graphene is not a major cause of the current change we observed because they should result in irreversible change in the current. With the small strain%

values used in our experiments, the adsorption site is also unlikely to be changed. This analysis leaves the strain-induced change of adsorption energy at the active sites as the most likely mechanism to explain our data. The density of the accessible active sites could also change due to the flattening of the graphene surface under tensile strain, slowing down the electron-transfer kinetics of graphene which will negatively impact the net change in the current.

Theoretical Results. To provide a molecular scale understanding of the experimental results, we have calculated the adsorption energy of H atoms on graphene as a function of strain using density functional theory (DFT) and explored the possibility that variations in H atom adsorption energies on strained graphene are responsible for the observed changes in current density. The calculations employ 3D periodic slab models and were done using the dispersion-corrected PBE-D3[27] density functional. As demonstrated by Davidson *et al*.,[28] when compared with other exchange-correlation functionals, PBE-D3 was found to provide the closest agreement to experimental data for physisorption energy of H on graphite. In this work we assume that this improved performance of PBE-D3 functional is transferrable to the case of chemisorption properties of H on graphite. Additional details of the computational setup used are provided in Computational Methods section.

The first objective of the computational investigations was to determine the adsorption energy of an H atom in the case of unstrained graphene and its dependence on coverage with a focus on the low coverage limit. Both these aspects are detailed in Figure 6. The dependence of the adsorption energy on coverage was established using a set of hexagonal supercells ranging from (2x2) to (8x8) in which a single H atom is adsorbed on unstrained graphene surface. This set of supercells allows to investigate a decrease in coverage from 1/8 ML in the case of the (2x2) supercell, to (1/50) ML for the (5x5) case, and further down to 1/128 ML for the (8x8) supercell.

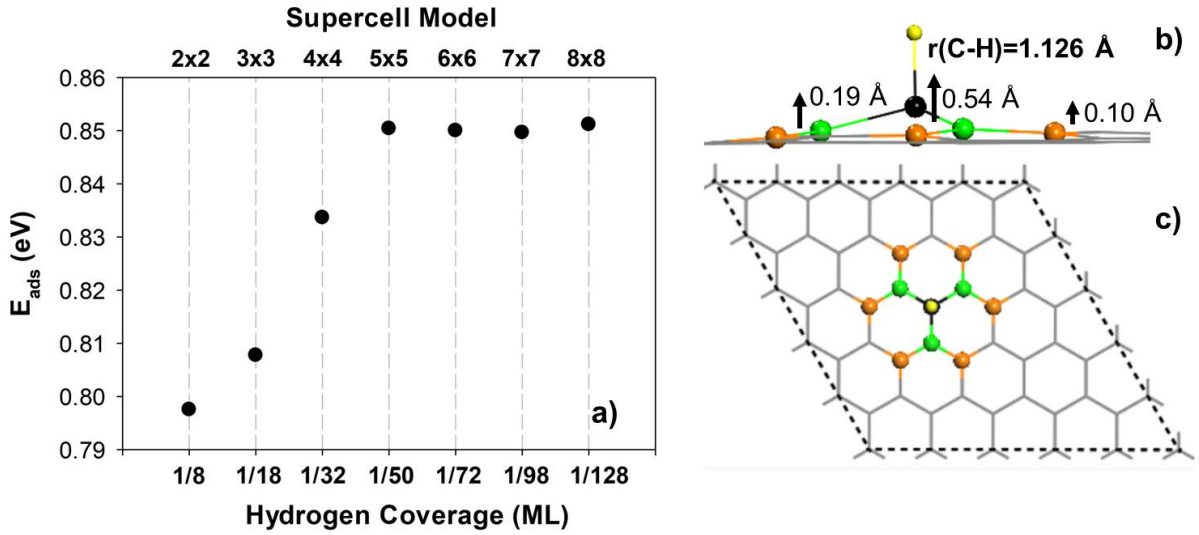

Figure 6. a) Variation with coverage of H adsorption energy on graphene at different coverages. The sum of energies of the bare graphene and of an isolated H atom was taken as the reference. Panels b) and c) indicate side and top views of the H adsorption configuration on-top a C site in the case of the (5x5) supercell model. In panel b) the upward displacements of the C atom to which the H is bonded (black colored) and its first (represented in green) and second (represented in brown) nearest neighbors are indicated. The H atom is shown with a yellow ball in panels b and c.

From the data in Figure 6a it can be seen that increase in supercell size leads to an increase in adsorption energy for the case of supercells ranging from (2x2) to (5x5) followed by a plateau in adsorption energies for supercells with larger lateral sizes. Based on this dependence it can be concluded that for the case of (5x5) supercell and the larger size supercells investigated, there is a minimal contribution of lateral interactions to H adsorption. The adsorption energy of 0.85 eV determined in this study for the case of the (5x5) supercell using PBE-D3 functional is comparable but slightly higher than the value of 0.84 eV reported by Casolo *et al*.[29] based on PBE functional without inclusion of long-range dispersion corrections. We also note that in Figure 6a the adsorption energy is expressed relative to the energy of the H atom. Positive adsorption energies correspond to stable configurations. For convenience, the same adsorption energy expressed relative to the energy of molecular H_2 (1/2 $E(H_2)$) is provided in Figure S4. Relative to the sum of energies for the bare graphene molecule and H_2 molecule, the adsorption energy of atomic H on

graphene is found to be a negative value, indicating an endothermic character for adsorption relative to the selected reference state.

Details of the binding configuration of the H atom in the (5x5) supercell are shown in Figure 6b from which it is seen that H adsorbs on-top of a C atom with a CH bond length of 1.126 Å. Adsorption takes place with sizable upward displacement of the C atom to which the H atom is bound (represented as a black ball in Figure 6b as well as its first and second nearest neighbors (shown as green and orange balls in Figure 6b and 6c. For the C atom to which the H atom is bound this displacement is calculated to be of 0.54 Å. A similar displacement of 0.59 Å was reported by Casolo *et al.*[29] for the case of H binding on graphene in a (5x5) supercell.

The second objective of the computational investigations was to determine the dependence of the H adsorption energy on the amount of surface strain. Motivated by the independence of the H adsorption energy on lateral interactions for the case of the (5x5) supercell identified above, we selected this supercell (or supercells with similar sizes as described below) for these calculations. In order to evaluate the variation of the adsorption energy for different levels of tensile strain applied to the graphene lattice two different supercell models have been considered as detailed in Figure S5. The first one corresponds to a (5x5) hexagonal supercell with a single H atom adsorbed on-top a carbon site, similar to that depicted in Figure 6c. Details of this model, the system of axes used and directions for lattice expansions are provided in supplementary Figure S5a. Specifically, a first type of lattice expansion was taken along a zigzag crystallographic direction conveniently chosen to be parallel to the selected Cartesian Ox axis (see Figure S5a) and hereafter denoted as (Zg,x). The second stretch direction was also taken along a zigzag direction but rotated 60° relative to (Zg,x) and hereafter denoted as (Zg,d) (see Figure S5a). In our hexagonal supercell setup model having (**u**1,**u**2) as hexagonal unit vectors, lattice elongations along the (Zg,x) direction involve tensile strain applied only along $\mathbf{u}_1$ hexagonal direction while extension of the lattice along (Zg,d) direction involves simultaneous tensile strains of equal sizes along both $\mathbf{u}_1$ and $\mathbf{u}_2$ hexagonal directions. The second model considered (see Figure S5b) consists of an orthogonal (5x3) supercell with

axes parallel to Cartesian Ox and Oy axes and oriented along the zigzag and armchair crystallographic directions, respectively. In this case, the tensile strain was applied only along Oy direction which was taken to be parallel to the armchair crystallographic direction, and hereafter indicated with the (Arm,y) acronym.

A summary of the results corresponding to variation of H adsorption energy on graphene for the case of lattices expanded along (Zg,x), (Arm,y) and (Zg,d) directions is presented in Figure 7. Lattice elongations up to 5% are considered.

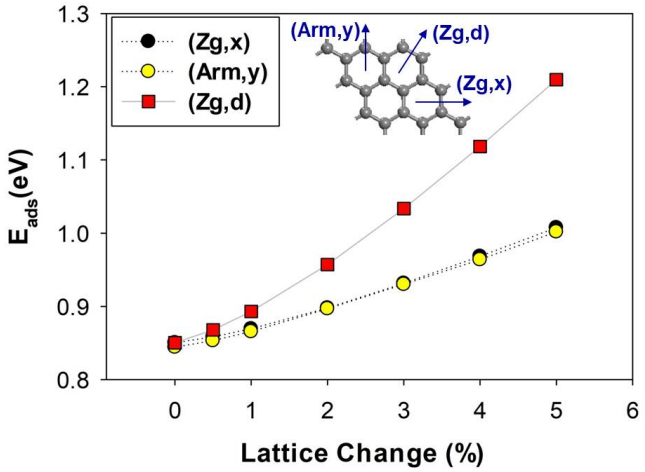

Figure 7. Variation of the H adsorption energy on graphene for lattice elongations along the zigzag (Zg,x), (Zg,d) and armchair (Arm,y) crystallographic directions.

As shown in this figure, for each of the three directions considered, stretching the graphene lattice leads to increase in the H adsorption energy. Individual energy changes however were found to depend on the displacement type. Specifically, for (Zg,x) and (Arm,y) displacements which involve elongations only along Cartesian Ox and Oy axes, respectively, the calculated adsorption energy values are practically superimposed and have similar overall variations. In contradistinction, the expansion along (Zg,d) direction which involves simultaneous stretches of similar sizes along both $\mathbf{u}_1$ and $\mathbf{u}_2$ hexagonal directions leads to

larger adsorption energy changes. In fact, it can be seen that adsorption energy for a given displacement along (Zg,d) direction is almost equal to the one along either (Zg,x) or (Arm,y) directions but at a displacement twice as large as the one considered for (Zg,d) direction. These results indicate not only an increase in adsorption energy of H with lattice expansion but they also demonstrate that when involving simultaneous displacements along $\mathbf{u}_1$ and $\mathbf{u}_2$ hexagonal axes, the effect on adsorption energies is practically twice that for single axis displacement (Zg,x) of an equal amount.

Graphene lattice expansion induces changes not only on the adsorption energy of H but also on its binding distance and vibrational properties. In particular, consistent with the increase in adsorption energy, the H atom is pulled closer to the graphene surface, as can be seen in Figure S6a where a systematic decrease in r(C-H) bond distance is observed with increasing amount of lattice stretch. These modifications take place with a corresponding blue shift of the ν(C-H) stretch vibration as shown in Figure S6b. Additionally, there are also changes in electronic properties of the system. Specifically, as seen in Figure 8 upon H adsorption on the graphene surface a new peak is observed in the density of states near the Fermi level originating from hybridization of C(2s) and C(2p) orbitals and associated mixing with H(1s). Stretching of the graphene lattice along (Zg,x) direction leads to an increase in electronic density corresponding to the occupied states of the C atom engaged in the CH bond just below the Fermi level. The electronic property modifications also extend to the work function of the system which increases with amount of lattice deformation (see Figure S7) as well as the p-band center (ε_p) of the graphene substrate which is shifted closer toward the Fermi level (see Figure S8), indicating a catalytically more active system.

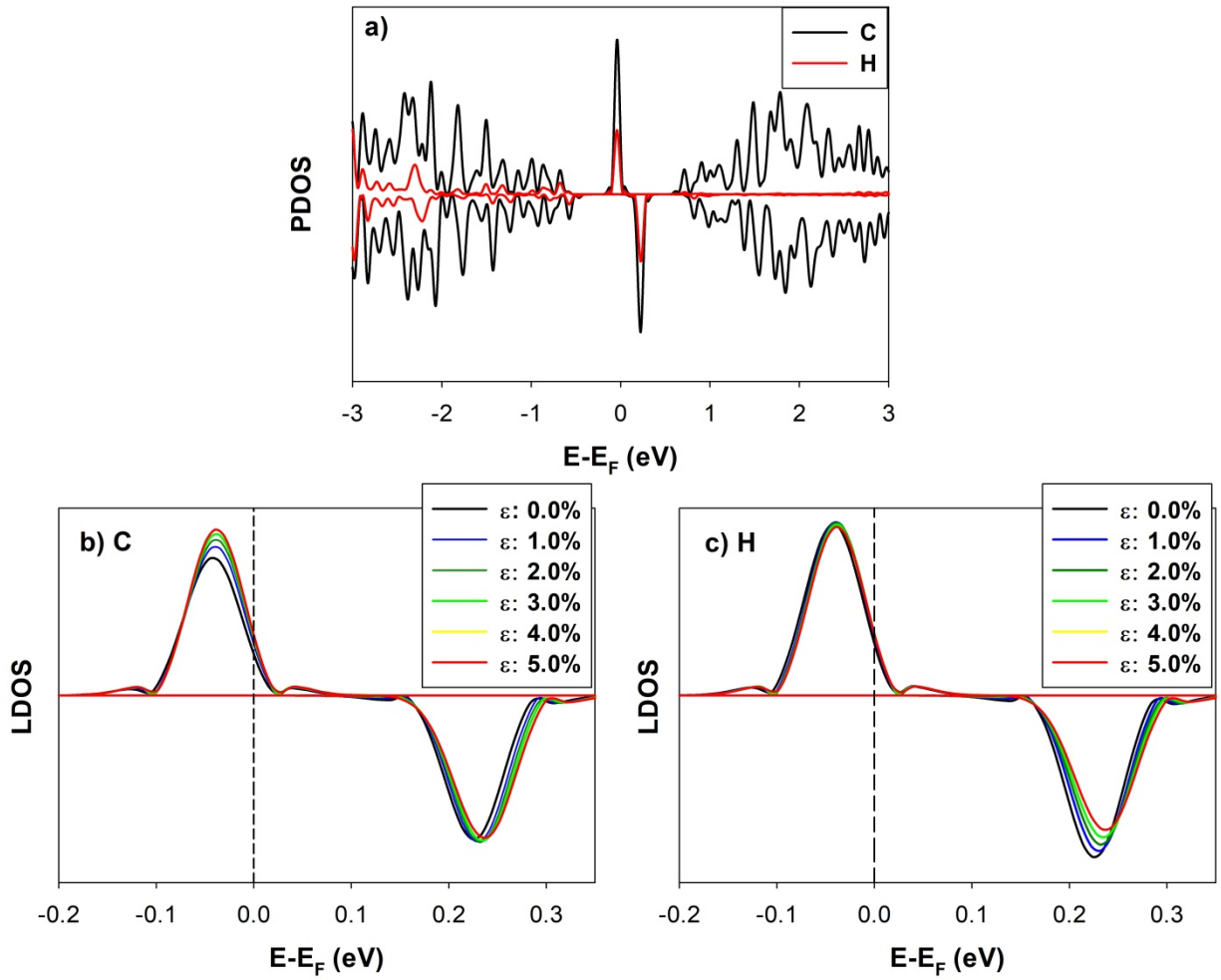

Figure 8. a) Projected density of states PDOS for the graphene C atoms and the adsorbed H atom in the case of un-stretched lattice. Details of the local density of states (LDOS) for the case of the bonding C atom and the H adsorbate as function of the lattice strain (ε) along (Zg,x) direction expressed in percentage form are detailed in panels b) and c), respectively.

For the bare graphene surface our measured Raman results from Figure 2 showed a red shift of the 2D peak with applied tensile stress. We have performed a similar theoretical analysis of vibrational frequencies shifts for the same range of stress values as determined experimentally. The calculated value of the in-plane D vibration of graphene changes from 1363 cm^{-1} for the unstretched lattice to 1358 cm^{-1} and

1355 cm^{-1} for the lattice stretched by 0.17% and 0.25%, respectively. When scaled by a 0.985 factor recommended for the PBE functional,[30] the second order overtones of these vibrations become 2685.1, 2675.2 and 2669.3 cm^{-1}, respectively These values can be compared with experimental results for the graphene 2D values in Figure 2. At zero strain, a very good agreement within 2.9 cm^{-1} is found between the calculated and experimental 2D frequency values. This agreement is maintained upon strain increase, with the calculated frequencies being within 2.3 cm^{-1} of the experimental values of 2673 cm^{-1} at 0.17% and 2667 cm^{-1} at 0.25% tensile strains, respectively.

A final aspect investigated is the influence of the enhanced bonding between H and graphene as a result of tensile strain upon HER. This reaction is generally described by a stepwise mechanism[31] which involves in the initial step a proton-coupled electron transfer reaction (Volmer reaction, see Eq(1))leading to adsorption of H on the electrocatalyst surface. In a subsequent step, desorption of molecular H_2 takes place via a Heyrovsky reaction (Eq.(2)) or a Tafel reaction (Eq. (3)). Independent of atomistic details of the mechanism involved, computational evaluation of the thermochemistry for reaction corresponding to atomic hydrogen bonding to the surface has proven to be a useful tool to compare HER activity of different catalysts.[32] In this work we followed a similar procedure and evaluate the free energy (ΔG_{H*}) for bonding reaction of H on graphene by including the adsorption energy changes (ΔE_H), the corresponding vibrational zero point energy (ΔZPE), entropic ($T\Delta S_H$) and the integrated heat capacity up to 298 K ($\Delta H_{0\rightarrow 298.15}$) corrections. The list of this set of corrections is detailed in Table S1. The corresponding calculated free energy diagram for hydrogen evolution on graphene surface under tensile strain is shown in Figure 9 for the case of lattice deformations along (Zg,x) direction, while similar results obtained for deformations along (Zg,d) are illustrated in Figure S9.

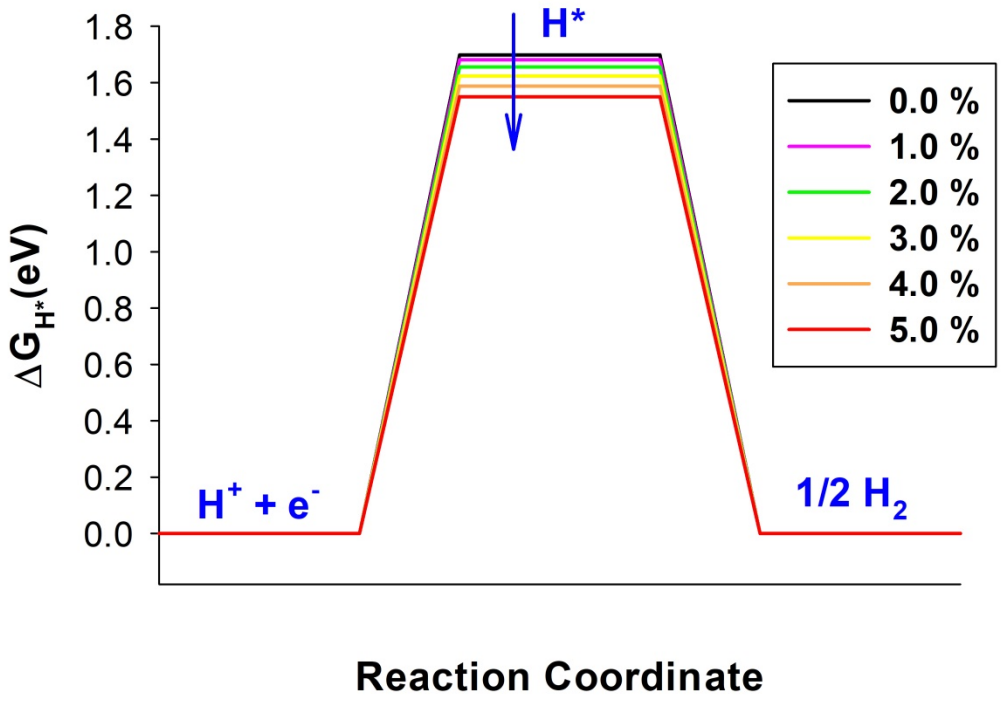

Figure 9. Variation of free energy ΔG_{H^*} for reaction * + H^+ + e^- ↔ H* on graphene at equilibrium (U=0) and standard conditions under different lattice expansions along (Zg,x) direction.

Ideal electrocatalysts for the HER reaction should have ΔG_{H^*} values as close as possible to zero. From this perspective, as seen in Figure 9, the bare unstretched graphene presents a relatively high and positive ΔG_{H^*} value, indicating a small HER activity. Relevant for the experimental results reported in this work is the fact that computational results in Figure 9 and Figure S10 demonstrate a systematic decrease in ΔG_{H^*} values when graphene lattice is stretched in the range 0-5 %. In particular, when considering the range of small elongations (0-0.25) % along (Zg,x) which encompasses the experimental strain range considered in this work, a fitted dependency of the calculated free energies changes from Table S1a of the form $\Delta G(\varepsilon)(eV)=1.698621 - 0.001970\ \varepsilon - 0.03000\ \varepsilon^2$ was determined, where ε represents the amount of lattice strain expressed in percentage form. The drop in ΔG_{H^*} values as shown in Figure 9 will lead to an increase

in HER activity and of the measured current density similar to our experimental findings. The increase in current density can be obtained based on the general relationship between the exchanged current and ΔG_{H^*} value as obtained by Kurapati *et.al*.[31] Following their work, the corresponding change of reaction rate at equilibrium is found to be proportional to $e^{\left(-\frac{\Delta G_{H^*}}{2RT}\right)}$. Based on this expression, one can estimate current density increases of 2.4% and 4.7% for lattice expansions of 0.17%, and 0.25%, respectively. Both of these theoretical estimates compare reasonably well with the measured current density increases determined in this study, which are 1.3 ± 0.2 % and 2.9 ± 0.5 % with 0.17 % and 0.25 % tensile strain, respectively. Possible reasons for the slight overestimation of the current density increase in calculations relative to the corresponding measured values might be the polycrystalline nature of graphene composed of large flakes in experiments and an anisotropic stress distribution. Stress anisotropy can be due to several factors including the flatness degree of the PET support and functional chemical groups existent on the support which can modify the coupling of PET support and graphene leading to an initial localized stress on graphene or possible slippage or inefficient strain transfer from the substrate. Additionally, the edge effects of graphene flakes and the quality of graphene layer itself can bring their own contributions as different types of surface defects can also modify the local stresses.

In summary, our combined experimental and computational analysis demonstrates that adsorption energy of H on graphene is enhanced by applying tensile strain which in turn leads to a drop in the associated free energy change corresponding to HER. The calculated variation in ΔG_{H^*} correlates well with the shift in the C p-band center of graphene (see Figure S10), demonstrating again the usefulness of this descriptor for correlating catalytic activity with electronic structure properties.[33] Furthermore, the good overall agreement between the calculated and measured current density variations with the amount of tensile strain support the interpretation that the increase in the H adsorption energy on graphene with stretching is responsible for the observed changes in HER reactivity. Graphene can sustain up to 20% of strain, much larger than the values considered here, without breaking. In addition, nitrogen-doped carbon electrodes

have shown exciting potential in various electrocatalytic reactions. Thus, strain engineering offers a promising approach to enhance the electrocatalytic activity of other carbon-based materials.

Methods

Graphene CVD synthesis and transfer. Graphene was grown on copper foils using chemical vapor deposition (CVD) based on previously reported method.[34] Copper foil (No. 46986, Alfa Aesar) was cut into approximately 1.5 cm × 6 cm strips and electropolished similar to the previously reported electropolishing method.[35] In brief, copper foil is electrolyzed with the current limit of 0.5 A for 30 s in phosphoric acid solution (500 ml of deionized water, 250 ml of phosphoric acid, 250 ml ethanol, 50 ml isopropyl alcohol, and 5 g of urea). Copper foil was used for both anode and cathode electrode, but only polished anode copper foil was used for graphene growth. After the electropolishing treatment, copper foil was thoroughly rinsed with deionized water, blow dried with nitrogen gas, and placed into a 1-inch-diameter fused quartz tube furnace. The tube was pump down to the base pressure <50 mTorr and back filled with H_2 (2 standard cubic centimeters per minutes (sccm)). The tube pressure with H_2 flow was maintained at ~200 mTorr. The furnace temperature was ramped to 1050 °C and annealed for >1 h under H_2. CH_4 (0.4 sccm, P_{total} ~230 mTorr) was introduced after the annealing step for ~30 min (growth), and the furnace was cooled rapidly to room temperature with the same gas flow for both H_2 and CH_4.

After the synthesis, graphene was transferred on to Polyethylene Terephthalate (PET, No. 365-144-58, Goodfellow) or SiO_2/Si wafer (thermal oxide, 300 nm, Addison Engineering) using a wet transfer technique.[36] In a typical transfer, as grown graphene on top of Cu foil was spin coated with 5 wt% Poly(methyl methacrylate) solution (PMMA, MW 996000 Aldrich) in anisole (99 %, Sigma-Aldrich). After the PMMA was coated on top of the graphene layer, the Cu foil was etched in fresh 0.1 M of aqueous ammonium persulfate solution (98 %, Sigma-Aldrich) for > 6 h. The PMMA/graphene film was scooped out with a clean glass slide and transferred into multiple water baths to rinse off the etchant and finally

placed on the target substrate. Transferred samples were dried in air over night or spin dried at 5000 rpm for 4 min. Centrifugal force from the spin-drying method did not have any noticeable added strain on the prepared graphene samples based on the Raman spectroscopy. PMMA layer was removed in an acetone bath for 1 h followed by another acetone bath for >6 h.

Raman spectroscopy. A custom-built micro-Raman spectrometer with 532 nm CW single-longitudinal mode solid state laser and Nikon S Plan Fluor ELWD 40x objective (NA: 0.60, WD: 3.6-2.8 mm) was used. The laser power was kept low (< 1 mW) to eliminate any photothermal heating effect. Laser power was measured at the sample stage before each experiment run.

Electrochemical measurements. All electrochemistry measurements were performed using Reference 600 potentiostat from Gamry instruments. Ground was set to float for the potentiostat. Electrochemical three electrode cell was constructed using platinum wire as a counter electrode and silver/silver chloride as a reference electrode. Typical area of working electrode was ~ 1 – 2 cm^2, and distance between electrodes were approximately 3 - 4 cm. (NOTE: platinum can be a significant contamination source in high current density electrochemical cells and should be carefully considered before use)[37, 38] Graphene electrode was attached to copper wire using silver paste (#12686-15, Electron Microscopy Sciences). Any exposed silver paste and copper wire surface were insulated by using high-vacuum silicone grease (Dow Corning). Sulfuric acid (95.0-98.0 %, Sigma-Aldrich) and Potassium Hexacyanoferrate(II) trihydrate (≥99.95 %, Sigma-Aldrich) solutions were prepared with ultrapure water (18.2 MΩ) from the Barnstead MicroPure system (Thermo Scientific).

Computational Methods. Adsorption of H on bare and stretched graphene has been analyzed using plane-wave spin-polarized DFT calculations with 3D periodic boundary conditions using the Vienna Ab Initio Simulation Package (VASP).[39, 40] The Perdew-Becke-Ernzerhof (PBE)[27] exchange-correlation functional corrected to include long-range van der Waals interactions using the D3 method of Grimme[41] with Becke-Johnson damping[42] has been used together with projector augmented wave (PAW) potentials of Blöch.[43, 44] The calculations also included dipole corrections as implemented in the VASP code.[45] A

cutoff energy of 1000 eV was used to expand the plane-wave basis set. The adsorption energy per H atom was determined using expression $E_{ads} = [(nE_{(H^*)}+E(_{slab})-(E_{(slab+nH^*)}]/n$, where n represents the number of H* atoms adsorbed on the surface in the supercell employed, $E_{(slab)}$ is the energy of the isolated slab and $E_{(slab+nH^*)}$ is the energy of the adsorbate/slab system. In the case of adsorption energies referenced with respect to H in atomic form, $E_{(H^*)}$ is taken to be the spin-polarized energy of a single H atom, while for adsorption energies referenced relative to molecular H_2, $E_{(H^*)}$ was taken to be ½ $E(H_2)$ for the optimized H_2 molecule. Positive adsorption energies obtained using the above formulas correspond to stable configurations.

The majority of calculations were performed using two different supercell models detailed in Figure S5. The first one (Figure S5a) consists of a 5x5 hexagonal supercell with (**u**1,**u**2) cell versors taken along zigzag crystallographic directions of graphene while the second model (Figure S5b) consists of a 5x3 orthogonal supercell with corresponding x and y cell directions taken along the zigzag (x) and armchair (y) directions. In both cases, a vacuum width of 16 Å in the direction perpendicular to the graphene surface was used to minimize the interactions with adjacent slabs. The dependence of adsorption energies on coverage was investigated using a set of hexagonal supercells ranging in size from 2x2 to 8x8. For the 5x5 hexagonal and 5x3 orthogonal supercells a (7x7x1) Monkhorst Pack[46] k-point grid was used to sample the Brillouin zone while for the (2x2)-(8x8) set of supercells the k-point grid sizes were scaled as indicated in Table S2.

The free energy changes corresponding to the hydrogen evolution reaction in acidic media at different stretching values of the graphene sheet were evaluated by including zero-point energy (ZPE), entropic and thermal corrections as detailed in Table S1. Evaluation of ZPE corrections was done by including contributions from the adsorbed H atom and from the bonding C atom and its first and second nearest neighbors. The free energy of $H^+ + e^-$ was taken to be that of ½ H_2 and the free energy of adsorbed H* was evaluated with respect to energy of ½H_2.

Data availability

Original data available upon request from the authors.

Supplementary Information

The Electronic Supplementary Information document contains additional experimental current density measurement data, tables of calculated free energies of reaction, details of calculation supercell model, additional theoretical results on C-H bond distance and vibrational frequency, work function of adsorbed H on graphene, C p-band center, free energy ΔG_{H^*} along different direction.

Materials & Correspondence

Corresponding Author

hliu@pitt.edu (H.L.) and jordan@pitt.edu (K.D.J.)

Author Contributions

[#] M.K. and D.C.S. contributed equally.

Acknowledgement

H.L. and K.D.J. acknowledge NSF (CBET-2028826) for partial support of this work. S.A. acknowledges NSF (CHE 1904258) for partial support of this work.

Author contributions

H.L. conceived the project and directed the experimental work with S.A.; M.L. conducted the experiments; D.C.S. and K.D.J. carried out the DFT simulations; M.L., D.C.S., and H.L. wrote the manuscript. All authors contributed to the revision of the manuscript.

Competing interests

None

References

1. Gsell, M.; Jakob, P.; Menzel, D., Effect of substrate strain on adsorption. *Science* **1998,** *280* (5364), 717-720.
2. Mavrikakis, M.; Hammer, B.; Norskov, J. K., Effect of strain on the reactivity of metal surfaces. *Physical Review Letters* **1998,** *81* (13), 2819-2822.
3. Kitchin, J. R.; Nørskov, J. K.; Barteau, M. A.; Chen, J. G., Modification of the surface electronic and chemical properties of Pt (111) by subsurface 3d transition metals. *The Journal of chemical physics* **2004,** *120* (21), 10240-10246.
4. Kitchin, J. R.; Nørskov, J. K.; Barteau, M. A.; Chen, J. G., Role of strain and ligand effects in the modification of the electronic and chemical properties of bimetallic surfaces. *Physical Review Letters* **2004,** *93* (15).
5. Kibler, L. A.; El-Aziz, A. M.; Hoyer, R.; Kolb, D. M., Tuning reaction rates by lateral strain in a palladium monolayer. *Angew. Chem.-Int. Edit.* **2005,** *44* (14), 2080-2084.
6. Hao, S. J.; Cui, L. S.; Jiang, D. Q.; Han, X. D.; Ren, Y.; Jiang, J.; Liu, Y. N.; Liu, Z. Y.; Mao, S. C.; Wang, Y. D.; Li, Y.; Ren, X. B.; Ding, X. D.; Wang, S.; Yu, C.; Shi, X. B.; Du, M. S.; Yang, F.; Zheng, Y. J.; Zhang, Z.; Li, X. D.; Brown, D. E.; Li, J., A Transforming Metal Nanocomposite with Large Elastic Strain, Low Modulus, and High Strength. *Science* **2013,** *339* (6124), 1191-1194.
7. Flynn, C. P., Strain-Assisted Epitaxial Growth of New Ordered Compounds. *Physical Review Letters* **1986,** *57* (5), 599-602.
8. Li, J.; Zhao, Z.; Ma, Y.; Qu, Y., Graphene and Their Hybrid Electrocatalysts for Water Splitting. *ChemCatChem* **2017,** *9* (9), 1554-1568.
9. Lee, C.; Wei, X.; Kysar, J. W.; Hone, J., Measurement of the Elastic Properties and Intrinsic Strength of Monolayer Graphene. **2008,** *321* (5887), 385-388.
10. Xie, A.; Xuan, N.; Ba, K.; Sun, Z., Pristine Graphene Electrode in Hydrogen Evolution Reaction. *ACS Appl Mater Interfaces* **2017,** *9* (5), 4643-4648.
11. Garcia-Miranda Ferrari, A.; Brownson, D. A. C.; Banks, C. E., Investigating the Integrity of Graphene towards the Electrochemical Hydrogen Evolution Reaction (HER). *Sci Rep* **2019,** *9* (1), 15961.
12. Boukhvalov, D. W.; Son, Y. W., Covalent Functionalization of Strained Graphene. *Chemphyschem* **2012,** *13* (6), 1463-1469.
13. Bissett, M. A.; Konabe, S.; Okada, S.; Tsuji, M.; Ago, H., Enhanced Chemical Reactivity of Graphene Induced by Mechanical Strain. *ACS Nano* **2013,** *7* (11), 10335-10343.
14. Ferrari, A. C.; Meyer, J. C.; Scardaci, V.; Casiraghi, C.; Lazzeri, M.; Mauri, F.; Piscanec, S.; Jiang, D.; Novoselov, K. S.; Roth, S.; Geim, A. K., Raman spectrum of graphene and graphene layers. *Physical Review Letters* **2006,** *97* (18).
15. Ni, Z. H.; Yu, T.; Lu, Y. H.; Wang, Y. Y.; Feng, Y. P.; Shen, Z. X., Uniaxial Strain on Graphene: Raman Spectroscopy Study and Band-Gap Opening. *ACS Nano* **2008,** *2* (11), 2301-2305.
16. Huang, M.; Yan, H.; Chen, C.; Song, D.; Heinz, T. F.; Hone, J., Phonon softening and crystallographic orientation of strained graphene studied by Raman spectroscopy. *Proceedings of the National Academy of Sciences* **2009,** *106* (18), 7304-7308.
17. Mohiuddin, T. M. G.; Lombardo, A.; Nair, R. R.; Bonetti, A.; Savini, G.; Jalil, R.; Bonini, N.; Basko, D. M.; Galiotis, C.; Marzari, N.; Novoselov, K. S.; Geim, A. K.; Ferrari, A. C., Uniaxial strain in graphene by Raman spectroscopy:Gpeak splitting, Grüneisen parameters, and sample orientation. *Physical Review B* **2009,** *79* (20).
18. Bissett, M. A.; Izumida, W.; Saito, R.; Ago, H., Effect of Domain Boundaries on the Raman Spectra of Mechanically Strained Graphene. *ACS Nano* **2012,** *6* (11), 10229-10238.

19. Casiraghi, C.; Pisana, S.; Novoselov, K. S.; Geim, A. K.; Ferrari, A. C., Raman fingerprint of charged impurities in graphene. *Applied Physics Letters* **2007,** *91* (23), 3.

20. Tolman, N. L.; Mukai, J. M.; Wang, S.; Zito, A.; Luo, T.; Liu, H., The effect of physical adsorption on the capacitance of activated carbon electrodes. *Carbon* **2019,** *150*, 334-339.

21. Hurst, J. M.; Li, L.; Liu, H., Adventitious hydrocarbons and the graphite-water interface. *Carbon* **2018,** *134*, 464-469.

22. Chen, R.; Balla, R. J.; Li, Z.; Liu, H.; Amemiya, S., Origin of Asymmetry of Paired Nanogap Voltammograms Based on Scanning Electrochemical Microscopy: Contamination Not Adsorption. *Analytical Chemistry* **2016,** *88* (16), 8323-8331.

23. Chen, R.; Nioradze, N.; Santhosh, P.; Li, Z.; Surwade, S. P.; Shenoy, G. J.; Parobek, D. G.; Kim, M. A.; Liu, H.; Amemiya, S., Ultrafast Electron Transfer Kinetics of Graphene Grown by Chemical Vapor Deposition. *Angew. Chem. Int. Ed.* **2015,** *54* (50), 15134-15137.

24. Shinagawa, T.; Garcia-Esparza, A. T.; Takanabe, K., Insight on Tafel slopes from a microkinetic analysis of aqueous electrocatalysis for energy conversion. *Scientific Reports* **2015,** *5* (1), 13801.

25. Lafkioti, M.; Krauss, B.; Lohmann, T.; Zschieschang, U.; Klauk, H.; Klitzing, K. V.; Smet, J. H., Graphene on a Hydrophobic Substrate: Doping Reduction and Hysteresis Suppression under Ambient Conditions. *Nano Letters* **2010,** *10* (4), 1149-1153.

26. Wang, Q. H.; Jin, Z.; Kim, K. K.; Hilmer, A. J.; Paulus, G. L. C.; Shih, C.-J.; Ham, M.-H.; Sanchez-Yamagishi, J. D.; Watanabe, K.; Taniguchi, T.; Kong, J.; Jarillo-Herrero, P.; Strano, M. S., Understanding and controlling the substrate effect on graphene electron-transfer chemistry via reactivity imprint lithography. *Nature Chemistry* **2012,** *4* (9), 724-732.

27. Perdew, J. P.; Burke, K.; Ernzerhof, M., Generalized gradient approximation made simple. *Physical Review Letters* **1996,** *77* (18), 3865-3868.

28. Davidson, E. R. M.; Klimeš, J.; Alfè, D.; Michaelides, A., Cooperative Interplay of van der Waals Forces and Quantum Nuclear Effects on Adsorption: H at Graphene and at Coronene. *ACS Nano* **2014,** *8* (10), 9905-9913.

29. Casolo, S.; Løvvik, O. M.; Martinazzo, R.; Tantardini, G. F., Understanding adsorption of hydrogen atoms on graphene. *The Journal of Chemical Physics* **2009,** *130* (5), 054704.

30. Computational Chemistry Comparison and Benchmark DataBase. Precomputed vibrational scaling factors. https://cccbdb.nist.gov/vibscalejust.asp (accessed March 25, 2021).

31. Kurapati, N.; Buoro, R. M.; Amemiya, S., Perspective—Beyond the Century-Long Paradigm of Hydrogen Electrochemistry through the Laviron–Amatore Paradox. *J. Electrochem. Soc.* **2020,** *167* (14), 146514.

32. Hinnemann, B.; Moses, P. G.; Bonde, J.; Jørgensen, K. P.; Nielsen, J. H.; Horch, S.; Chorkendorff, I.; Nørskov, J. K., Biomimetic Hydrogen Evolution: MoS_2 Nanoparticles as Catalyst for Hydrogen Evolution. *J. Am. Chem. Soc.* **2005,** *127* (15), 5308-5309.

33. Nilsson, A.; Pettersson, L. G. M.; Hammer, B.; Bligaard, T.; Christensen, C. H.; Nørskov, J. K., The electronic structure effect in heterogeneous catalysis. *Catalysis Letters* **2005,** *100* (3), 111-114.

34. Li, X. S.; Cai, W. W.; An, J. H.; Kim, S.; Nah, J.; Yang, D. X.; Piner, R.; Velamakanni, A.; Jung, I.; Tutuc, E.; Banerjee, S. K.; Colombo, L.; Ruoff, R. S., Large-Area Synthesis of High-Quality and Uniform Graphene Films on Copper Foils. *Science* **2009,** *324* (5932), 1312-1314.

35. Chen, S. S.; Ji, H. X.; Chou, H.; Li, Q. Y.; Li, H. Y.; Suk, J. W.; Piner, R.; Liao, L.; Cai, W. W.; Ruoff, R. S., Millimeter-Size Single-Crystal Graphene by Suppressing Evaporative Loss of Cu During Low Pressure Chemical Vapor Deposition. *Advanced Materials* **2013,** *25* (14), 2062-2065.

36. Li, X. S.; Zhu, Y. W.; Cai, W. W.; Borysiak, M.; Han, B. Y.; Chen, D.; Piner, R. D.; Colombo, L.; Ruoff, R. S., Transfer of Large-Area Graphene Films for High-Performance Transparent Conductive Electrodes. *Nano Letters* **2009,** *9* (12), 4359-4363.

37. Tian, M.; Cousins, C.; Beauchemin, D.; Furuya, Y.; Ohma, A.; Jerkiewicz, G., Influence of the Working and Counter Electrode Surface Area Ratios on the Dissolution of Platinum under Electrochemical Conditions. *ACS Catalysis* **2016,** *6* (8), 5108-5116.

38. Bird, M. A.; Goodwin, S. E.; Walsh, D. A., Best Practice for Evaluating Electrocatalysts for Hydrogen Economy. *ACS Applied Materials & Interfaces* **2020,** *12* (18), 20500-20506.

39. Kresse, G.; Furthmüller, J., Efficiency of ab-initio total energy calculations for metals and semiconductors using a plane-wave basis set. *Computation Materials Science* **1996,** *6* (1), 15-50.

40. Kresse, G.; Furthmüller, J., Efficient iterative schemes for ab initio total-energy calculations using a plane-wave basis set. *Physical Review B* **1996,** *54* (16), 11169-11186.

41. Grimme, S., Semiempirical GGA-type density functional constructed with a long-range dispersion correction. *Journal of Computational Chemistry* **2006,** *27* (15), 1787-1799.

42. Grimme, S.; Ehrlich, S.; Goerigk, L., Effect of the Damping Function in Dispersion Corrected Density Functional Theory. *Journal of Computational Chemistry* **2011,** *32* (7), 1456-1465.

43. Blöchl, P. E., Projector augmented-wave method. *Physical Review B* **1994,** *50* (24), 17953-17979.

44. Kresse, G.; Joubert, D., From ultrasoft pseudopotentials to the projector augmented-wave method. *Physical Review B* **1999,** *59* (3), 1758-1775.

45. Neugebauer, J.; Scheffler, M., Adsorbate-substrate and adsorbate-adsorbate interactions of Na and K adlayers on Al(111). *Physical Review B* **1992,** *46* (24), 16067-16080.

46. Monkhorst, H. J.; Pack, J. D., Special points for Brillouin-zone integrations. *Physical Review B* **1976,** *13* (12), 5188-5192.

For Table of Contents Only